Geophysical Journal International

*Geophys. J. Int.* (2013) **192,** 1–6 doi: 10.1093/gji/ggs002

# High-velocity anomaly adjacent to the western edge of the Pacific low-velocity province

Koki Idehara,[1] Satoru Tanaka[2] and Nozomu Takeuchi[3]

[1]*Department of Earth and Planetary Science, University of Tokyo,* 7–3-1 *Hongo, Bunkyo-ku, Tokyo* 113–0033, *Japan. E-mail: idehara@eps.s.u-tokyo.ac.jp*
[2]*Institute for Research on Earth Evolution, Japan Agency for Marine-Earth Science and Technology,* 2–15, *Natsushima-cho, Yokosuka* 237–0061, *Japan*
[3]*Earthquake Research Institute, University of Tokyo,* 1–1-1 *Yayoi, Bunkyo-ku, Tokyo* 113–0032, *Japan*

Accepted 2012 September 3. Received 2012 September 3; in original form 2012 January 24

## SUMMARY

ScS–S differential traveltimes of shear waves traversing the lowermost mantle beneath New Guinea and the Banda Sea, in nearly north–south and east–west directions for different source–array pairs, exhibit a pronounced fast shear-wave velocity anomaly at the western edge of the Pacific Large Low-Shear-Velocity Province (LLSVP). Forward modelling of the differential time residuals for both sets of ray paths reveals an increase in shear velocity of around 1 per cent adjacent to the LLSVP, which has a low-velocity anomaly of −1.5 per cent, at a lateral boundary at 137°E. The marked increase in shear velocity at the edge of the LLSVP possibly indicates the presence of subducted slab material, which may reside adjacent to the LLSVP pile, resulting from pushing and sweeping of the pile into the region beneath the central Pacific.

**Key words:** Mantle processes; Body waves; Dynamics: convection currents, and mantle plumes; Pacific Ocean.

## 1 INTRODUCTION

Recent studies based on global tomography and geological mapping have suggested that at least some of the surface hotspots and Large Igneous Provinces (LIPs) are likely to be derived from deep mantle plumes that originated at the D″ region near strong lateral shear velocity gradients (e.g. Thorne *et al.* 2004; Torsvik *et al.* 2006). This urges us to focus on the regions of strong lateral gradients in shear velocity in the D″ layer, in terms of thermochemical anomalies and the generation of deep mantle plumes.

Seismological observations have revealed extensive regions of considerably reduced shear velocity in the deep mantle beneath Africa and the central Pacific (e.g. Ritsema *et al.* 1998; He *et al.* 2006). These two Large Low-Shear-Velocity Provinces (LLSVPs) are characterized by their sharp lateral boundaries in shear velocity (e.g. Ritsema *et al.* 1998; To *et al.* 2005), and have been considered to be chemically distinct regions. Furthermore, several recent numerical simulations have indicated that the LLSVPs physically interact with subducted slab material at the bottom of the mantle, with downwellings shaping thermochemical piles and deep mantle plumes originating from instabilities at the edges of the piles (e.g. Nakagawa & Tackley 2011; Tan *et al.* 2011).

However, the detailed seismic velocity structure around the edges of the LLSVPs remains largely unknown. Many previous studies utilized rays that propagated mainly through these regions in a certain direction, criss-crossing the LLSVP boundary (e.g. He *et al.* 2006; Takeuchi *et al.* 2008). Limited azimuthal coverage blurs the resolution of velocity structure surrounding the LLSVP. In this study, we address this issue by analysing the traveltimes of shear waves traversing the deep mantle both parallel and perpendicular to the boundary of the LLSVP, and thereby providing improved bounds on shear velocity anomalies in and around the LLSVP, as well as its geographical boundary.

## 2 DIFFERENTIAL TRAVELTIME RESIDUALS OF ScS–S

We consider two sets of source–array pairs (Fig. 1). The first set comprises earthquakes in and around the Japan Islands, and broadband seismic stations in Australia and the South Pacific, resulting in 230 paths. The rays propagate approximately north–south (herein referred to as N–S paths). The second set, for which the paths are approximately east–west, comprises earthquakes in Vanuatu and Fiji–Tonga Islands, and stations in Vietnam and South China, resulting in 68 paths (herein, E–W paths). Part of the data for the E–W paths has been described by Takeuchi *et al.* (2008). Because the boundary of the LLSVP is oriented approximately north–south in the study area (Fig. 1), the N–S and E–W paths propagate along and across the boundary, respectively. The ScS phases sample the D″ region beneath 10°S–10°N in latitude and 130°E–150°E in longitude.

We analyse the transverse component of displacement seismograms. All traces are band-pass filtered between 5 and 100 s, and the differential traveltimes of ScS–S are measured using the cross-correlation method. The differential time residuals are calculated

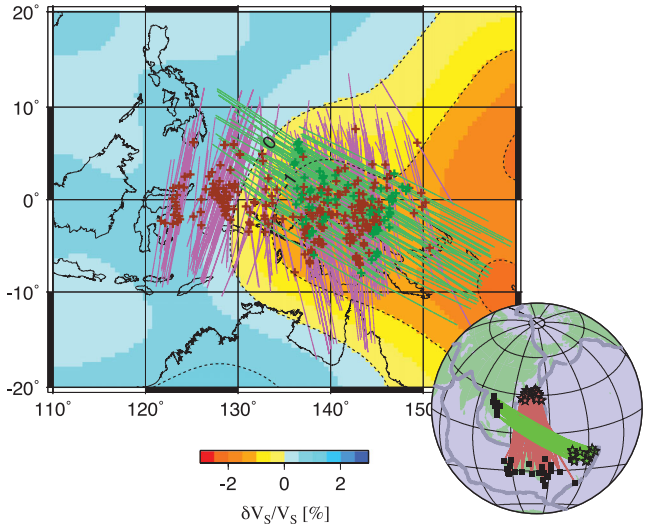


**Figure 1.** Map of the area where the ScS rays sampled the D″ region. Crosses with lines show the ScS reflection points at the CMB and the paths where the ScS propagated through the lowermost 250 km of the mantle, computed using the PREM velocity model. The colours in pink and green denote the N–S and E–W paths, respectively. The background is an *S*-wave velocity model (contour interval, 1 per cent) in the lowermost mantle based on SB4L18 (Masters *et al.* 2000). The inset shows the source–receiver geometry for the N–S (pink) and E–W (green) paths. Stars and squares denote the events and the stations, respectively. Thick grey lines represent plate boundaries.

with respect to PREM (Dziewonski & Anderson 1981) at a reference period of 10 s, and then corrected for Earth's ellipticity following Dziewonski & Gilbert (1976). Residual errors are evaluated following Tanaka (2002), which are based on the widths of the S and ScS peaks at amplitude values equal to the peak amplitudes minus the pre-S rms noise (see Fig. S1 to illustrate examples of accepted and rejected waveforms). We retain those residuals with a reading error $\leq 2$ s. The resultant data set consists of 148 residuals for the N–S paths and 34 for the E–W paths (7 of the residuals are for sScS–sS). The epicentral distance ranges from 55° to 77° for the N–S paths and 66–83° for the E–W paths. The reflected/refracted phase at the D″ discontinuity (Sbc/Scd) is small in our data set, as referred in Takeuchi *et al.* (2008).

The contribution of heterogeneity above the lowermost 250 km of the mantle is corrected for using the following global *S*-wave tomography models: SB4L18 (Masters *et al.* 2000), SMEAN (Becker & Boschi 2002), SH18CEX (Takeuchi 2012), S362D1 (Gu *et al.* 2001) and TXBW (Grand 2002). The variances of the observed residuals are reduced substantially after the corrections for any one of the models, showing that all the models are valid to first order for removing the mantle contribution above the D″ region. In this study, we adopted the SB4L18 model, which yields the greatest reduction in variance.

Fig. 2 shows the residuals before and after correction for mantle heterogeneity. The patterns of positive and negative residuals are not significantly changed after correction, but the corrected residuals tend to become smaller in amplitude. A clear boundary between positive and negative residuals is observed for both the N–S and E–W paths. Interestingly, the longitude of the apparent boundary, as obtained from the N–S paths, appears to be located approximately 5° west of that obtained from the E–W paths. The residuals between 130° and 137°E for the N–S paths are highly scattered comparing with them in other longitude ranges, possibly because of complex geometry of the lateral velocity boundary, the 2-D or 3-D effects from the boundary, and/or strong fine-scale velocity anomalies in the boundary region. Note that the multipathing effect, which has been observed in several other lowermost mantle regions where rays sampled the LLSVP boundary (e.g. To *et al.* 2005; Sun *et al.* 2009), is not clear in our waveform data. It is possibly because our ScS data for the N–S paths are not grazing along the horizontal boundary due to the relatively small epicentral distances. Furthermore, our cross-correlation method is likely to discard the waveform data distorted by the multipathing effect. The example waveforms of ScS across the LLSVP boundary are shown as recording sections along the longitude direction in Fig. S2.

## 3 FORWARD MODELLING

We consider two blocks with different shear velocity perturbations, separated by a north–south boundary (see Fig. 3a). We examine the model fits by varying the following parameters: shear velocity anomalies in the eastern and western blocks ($\delta V_{\rm E}$, $\delta V_{\rm W}$, respectively) in the lowermost 250 km of the mantle, and the longitude of the boundary. Prior to the modelling, the residuals from the heterogeneity above the lowermost 250 km of the mantle are removed from the observed residuals. The calculated residuals due to mantle heterogeneity are simply integrated along 1-D ray paths calculated from PREM. The goodness-of-fit is assessed by the variance of the residual corrected for mantle heterogeneity (herein referred to as the final variance).

We examine the three initial cases summarized in Table 1. The boundary longitude in Case 1 (140°E) is identical to that inferred by Takeuchi *et al.* (2008). In Cases 2 and 3, the boundary longitude is shifted westward by 3° from that in Case 1. Case 3 is identical to Case 2 except for incorporations of a positive velocity anomaly in the western block ($\delta V_{\rm W} = 0.8$ per cent).

Figs 3a and 3b show the distributions of the calculated residuals for Cases 1–3 and their final variances, respectively. In Case 1, the distribution of the calculated residuals for the N–S paths is not consistent with that of the observed residuals: in contrast, those for the E–W paths show a good fit. On the other hand, the residual boundary becomes blurred for the E–W paths in Case 2. Only Case 3 generated residual patterns similar to the observed data for both the N–S and E–W paths.

The optimal values of the boundary longitude and the velocity contrast between the LLSVP and the adjacent mantle are determined by a grid search method, yielding $0.74 \pm 0.33$ per cent for $\delta V_{\rm W}$ and $-1.44 \pm 0.17$ per cent for $\delta V_{\rm E}$, with the boundary at 137 $\pm$ 0.6°E in longitude (Figs 3c and d). Note the presented uncertainties denote the 95 per cent confidence level. The best-fit values determined using the other tomography models are plotted for reference. In this study, however, we adopted the best-fitting model determined using the SB4L18 model as the preferred model since it provides the largest reduction in variance. Note that, even if we use the best-fitting models determined using the other four tomography models, the boundary is determined around 137°E and $\delta V_{\rm W}$ stays positive (Figs 3c and d), suggesting the robustness of our conclusions.

We further evaluate the model-data fits for a basal layer extracted from the SB4L18 model and the ones amplified by the scaling factor to examine how well the models explain the observed residuals comparing with our preferred model. However, none of the resultant variances are smaller than that for our preferred model (Fig. 3e).

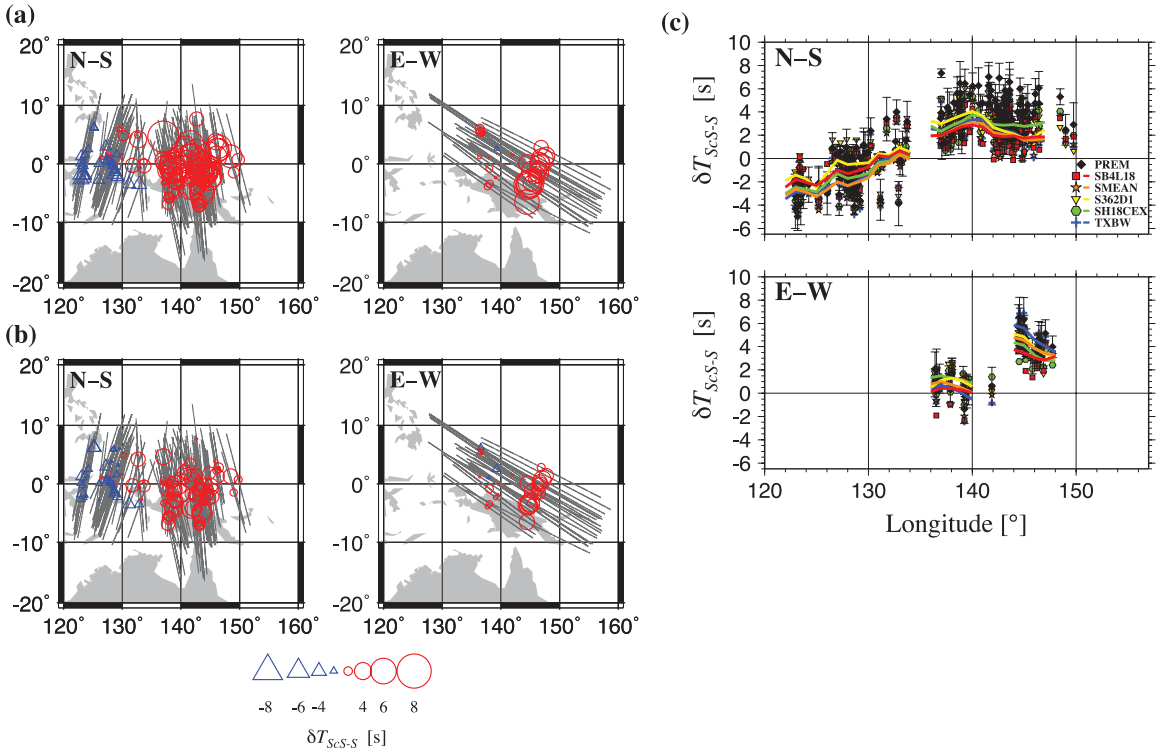


**Figure 2.** Observed traveltime residuals. (a) Map views of the residual distribution for the N–S and E–W paths. Residuals are plotted at the bounce points of ScS at the CMB. Circles and triangles represent positive and negative residuals, respectively. Residuals are not corrected for mantle heterogeneity above the D″ layer. (b) As for (a) but the residuals are corrected for mantle heterogeneity using the SB4L18 model. (c) Traveltime residuals shown as a function of longitude. Each coloured symbol indicates the residual corrected for mantle heterogeneity by each tomography model. Coloured lines show the moving-average residual with a window size of 2.5° in longitude. Solid diamonds with error bars denote the uncorrected (PREM) residuals with the reading errors.

In the SB4L18 model, the residual boundary becomes blurred for the E–W paths, while the positive residuals for the N–S paths show a good fit with the observed data. The model fit decreases significantly with amplifying the velocity anomaly in the SB4L18 model (Fig. 3e). These results indicate that the velocity increase in the vicinity of the low-velocity anomaly is not resolved well by the SB4L18 model. The distributions of the residuals corrected for the other tomography models and their best-scaled models are shown in Fig. S3, with their variances in Fig. S4. Although some of the best-scaled models improve the model fits significantly, those models fit less well than our preferred model.

## 4 DISCUSSION

Our analysis of the differential traveltime residuals shows that the western edge of the Pacific LLSVP is bounded by a fast-velocity anomaly of around 1 per cent in the D″ layer. The amplitude of this positive velocity anomaly is much larger than that evaluated from global tomography studies. On the other hand, Takeuchi *et al.* (2008) investigated in the same region using only E–W paths, and inferred a low-velocity anomaly in the LLSVP of down to −4 per cent, with a velocity identical to that of IASP91 (Kennett & Engdahl 1991) in the surrounding mantle. Our analysis can provide better constraints on the velocity anomalies of the LLSVP and the surrounding mantle, given that we combined with the N–S paths.

From the geodynamic point of view, the significant increase in shear velocity at the edge of the LLSVP may be explained in terms of the low temperature of a cold subducted slab. Global tomography studies have revealed an extensive fast-velocity anomaly beneath the western Pacific and eastern Eurasia (e.g. Masters *et al.* 2000; Fukao *et al.* 2009), interpreted as ancient subducted slabs (e.g. Fukao *et al.* 2009). This enhances the idea that the marked increase in shear velocity at the edge of the LLSVP is associated with subducted slab material. This structure may support the suggestion, based on the results of thermochemical simulations, that the LLSVP materials have been pushed and swept aside by the subducted slab material which resides adjacent to the LLSVP (e.g. McNamara & Zhong 2005; Nakagawa & Tackley 2011; Tan *et al.* 2011).

If compositional effects are negligible in the studied region, a very large temperature variation of over 500 K would be required to cause a shear velocity contrast evaluated in this study ($\geq \sim$2.2 per cent) for a lower mantle consisting of either perovskite or post-perovskite (Wentzcovitch *et al.* 2006). However, lateral variation in phase abundance of perovskite and post-perovskite may substantially reduce the required temperature variation (Lay *et al.* 2006). To tightly constrain the amount of temperature variation in this region, we need to locate the depth of the D″ discontinuity, which is an important future research topic.

## 5 CONCLUSIONS

We inferred lateral variations in shear-wave velocity across the western edge of the Pacific LLSVP using the differential traveltimes of ScS–S propagating parallel and perpendicular to the LLSVP boundary. An abrupt boundary between positive and negative residuals is clearly observed for both the parallel and perpendicular paths. Forward modelling of the residuals revealed that the observed residuals are best explained by a low shear velocity anomaly of −1.44 per

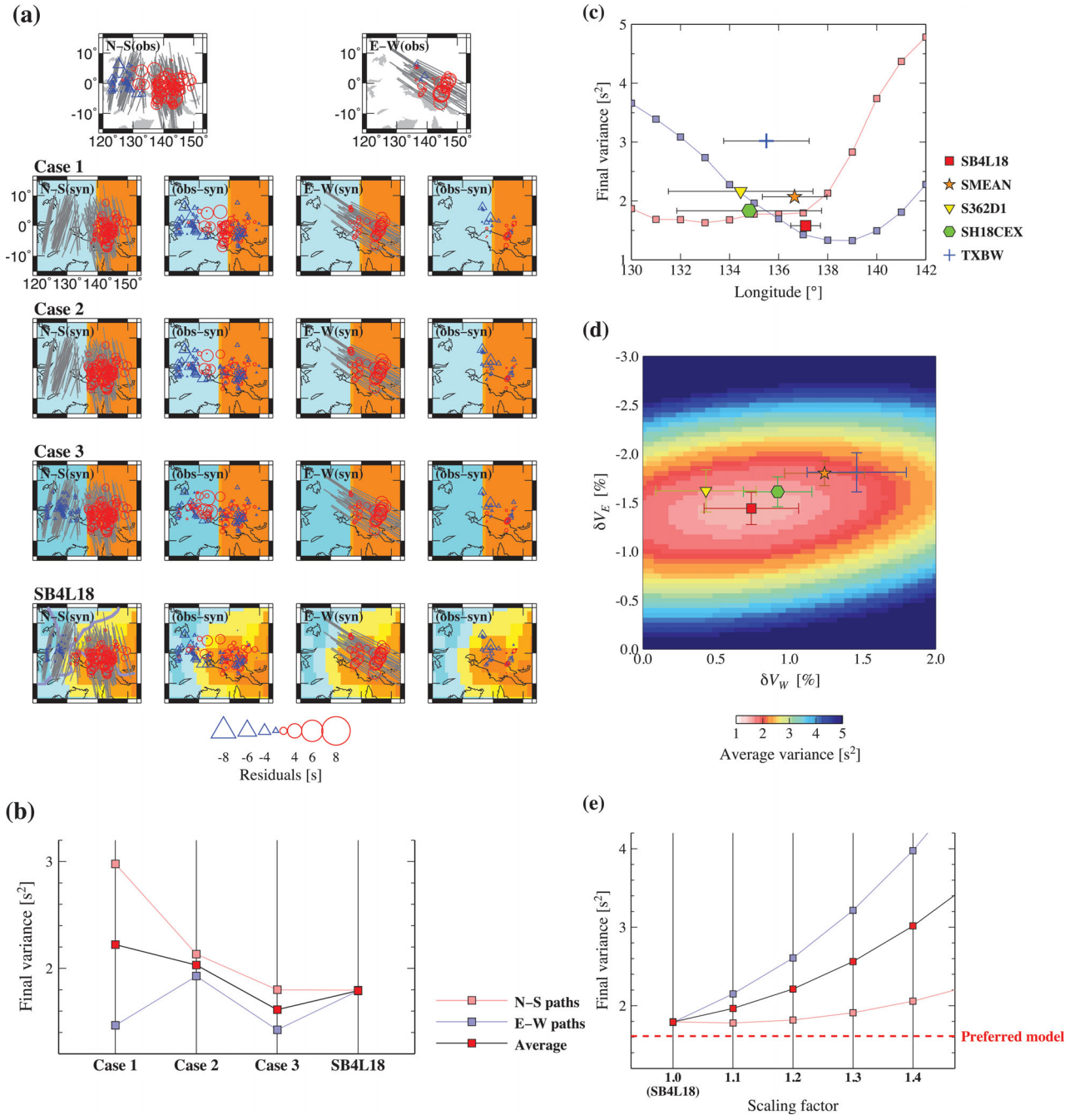


**Figure 3.** (a) Synthetic residuals of ScS–S (the first and third maps from the left-hand side) and the observed residuals subtracted by the synthetic residuals (the second and fourth from the left-hand side) for the N–S and E–W paths for Cases 1–3 and for the basal layer extracted from the SB4L18 model. The maps on the top show the distributions of the observed residuals for the N–S (left-hand panel) and E–W (right-hand panel) paths. Observed residuals are corrected for mantle structure using the SB4L18 model. Positive and negative residuals are plotted in the same manner as in Fig. 2a. The background colour represents the shear velocity anomalies for each case (the colour scale is the same as in Fig. 1) (b) Final variances for the N–S and E–W paths for Cases 1–3 and the SB4L18 model. Lines with squares in light pink, light blue, and red denote the variance for the N–S paths, E–W paths, and the average variance for the N–S and E–W paths, respectively (c) Variances for the longitude of the boundary between the LLSVP and the surrounding mantle, with $\delta V_E$ and $\delta V_W$ fixed to $-1.6$ and 0.8 per cent, respectively. The best-fitting values of longitude are determined by averaging the final variances for the N–S and E–W paths. The symbols with lines in light red and light blue indicate the variances for the N–S and E–W paths, respectively, corrected for the SB4L18 model. The minimum variances using the corresponding tomography models with 95 per cent confidence intervals are shown by symbols with error bars filled in colour (SB4L18: 137.1 $\pm$ 0.6°; SMEAN: 136.7 $\pm$ 1.3°; S362D1: 134.5 $\pm$ 3°; SH18CEX: 134.8 $\pm$ 3°; TXBW: 135.5 $\pm$ 1.8°). Errors are estimated based on bootstrap resampling (Efron & Tibshirani 1991) (d) Average variances for $\delta V_E$ and $\delta V_W$ with the lateral boundary determined in (c). The minimum variances with errors are represented in the same way as in (c). The optimal values with 95 per cent confidence intervals of $\delta V_W$ and $\delta V_E$ are: SB4L18: ($\delta V_W$, $\delta V_E$) = (0.74 $\pm$ 0.33 per cent, $-1.44$ $\pm$ 0.17 per cent); SMEAN: 1.24 $\pm$ 0.28 per cent, $-1.8$ $\pm$ 0.13 per cent; S362D1: 0.43 $\pm$ 0.35 per cent, $-1.62$ $\pm$ 0.22 per cent; SH18CEX: 0.92 $\pm$ 0.24 per cent, $-1.61$ $\pm$ 0.16 per cent; TXBW: 1.46 $\pm$ 0.35 per cent, $-1.81$ $\pm$ 0.20 per cent. The variance for each gridpoint is shown in the background, corrected for mantle heterogeneity using the SB4L18 model (e) Variances by changing the scaling factor for the amplitude of the velocity anomaly in the SB4L18 model. The final variances for the N–S, E–W, and the average residuals are denoted in the same manner as in (b).

**Table 1.** Conditions for the three cases.

| Case | Boundary long. (°E) | $\delta V_W$ (per cent) | $\delta V_E$ (per cent) |
|---|---|---|---|
| 1 | 140 | 0.0 | −1.6 |
| 2 | 137 | 0.0 | −1.6 |
| 3 | 137 | 0.8 | −1.6 |

cent in the LLSVP and a fast-velocity anomaly of 0.74 per cent in the adjacent mantle, with the lateral boundary at 137°E in longitude. The presence of a fast-velocity anomaly in the vicinity of the LLSVP may indicate a subducted slab material residing adjacent to the LLSVP pile after pushing and sweeping the piles into the region beneath the central Pacific.

## ACKNOWLEDGMENTS

The authors gratefully acknowledge the OHP DMC and IRIS Data Management System for supplying the waveform data. The S362D1 model and supporting code were kindly provided by Y. Gu, SB4L18 were downloaded from the Reference Earth Model (REM) website, and the SMEAN and TXBW models were downloaded from the website of the European Seismological Reference Model. We also thank T. Lay and A. Hutko for valuable review comments, which helped us improving our article. Figures were plotted using Generic Mapping Tools (Wessel & Smith 1995). HC software package (Becker & Boshi, 2002) was used to extract spherical harmonics solutions. This work was partly supported by a Grant-in-Aid for Scientific Research (Nos. 19104011 and 22000003), Japan Society for the Promotion of Science.

## REFERENCES

Becker, T.W. & Boschi, L., 2002. A comparison of tomographic and geodynamics mantle models, *Geochem. Geophys. Geosyst.,* **3,** 1003, doi:10.1029/2001GC000168.

Dziewonski, A.M. & Anderson, D.L., 1981. Preliminary reference earth model, *Phys. Earth planet. Inter.,* **25,** 297–356.

Dziewonski, A.M. & Gilbert, F., 1976. The effect of small, aspherical perturbations on travel times and a re-examination of the corrections for ellipticity, *Geophys. J. R. astr. Soc.,* **44,** 7–17.

Efron, B. & Tibshirani, R., 1991. Statistical data analysis in the computer age, *Science,* **253,** 390–395.

Fukao, Y., Obayashi, M., Nakakuki, T. & the Deep Slab Project Group, 2009. Stagnant slab: a review, *Annu. Rev. Earth planet. Sci.,* **37,** 19–46.

Grand, S.P., 2002. Mantle shear-wave tomography and the fate of subducted slabs, *Phil. Trans. R. Soc. Lond.,* **360,** 2475–2491.

Gu, Y.J., Dziewonski, A.M., Su, W. & Ekström, G., 2001. Models of the mantle shear velocity and discontinuities in the pattern of lateral heterogeneities, *J. geophys. Res.,* **106,** 11 169–11 200.

He, Y., Wen, L. & Zheng, T., 2006. Geographic boundary and shear wave velocity structure of the "Pacific anomaly" near the core-mantle boundary beneath western Pacific, *Earth planet. Sci. Lett.,* **244,** 302–314.

Kennett, B.L.N. & Engdahl, E.R., 1991. Traveltimes for global earthquake location and phase identification, *Geophys. J. Int.,* **105,** 429–465.

Lay, T., Hernlund, J., Garnero, E.J. & Thorne, M.S., 2006. A post-perovskite lens and D″ heat flux beneath the central Pacific, *Science,* **314,** 1272.

Masters, T.G., Laske, G., Bolton, H. & Dziewonski, A.M., 2000. The relative behavior of shear velocity, bulk sound speed, and compressional velocity in the mantle: Implications for chemical and thermal structure, in *Earth's Deep Interior. Mineral Physics and Tomography From the Atomic to the Global Scale,* Geophys. Monogr. Ser., pp. 63–86, eds Karato, S., Forte, A. M., Liebermann, R. V., Masters, T. G., Stixrude L., AGU, Washington, DC.

McNamara, A.K. & Zhong, S., 2005. Thermochemical structure beneath Africa and the Pacific Ocean, *Nature,* **437,** 1136–1139.

Nakagawa, T. & Tackley, P.J., 2011. Effects of low-viscosity post-perovskite on thermo-chemical mantle convection in a 3-D spherical shell, *Geophys. Res. Lett.,* **38,** L04309, doi:10.1029/2010GL046494.

Ritsema, J., Ni, S., Helmberger, D.V. & Crotwell, H.P., 1998. Evidence for strong shear velocity reductions and velocity gradients in the lower mantle beneath Africa, *Geophys. Res. Lett.,* **25,** 4245–4248.

Sun, D., Helmberger, D.V., Ni, S. & Bower, D., 2009. Direct measures of lateral velocity variation in the deep Earth, *J. geophys. Res.,* **114,** B05303, doi:10.1029/2008JB005873.

Takeuchi, N., Morita, Y., Xuyen, N.D. & Zung, N.Q., 2008. Extent of the low-velocity region in the lowermost mantle beneath the western Pacific detected, by the Vietamese Broadband Seismograph Array, *Geophys. Res. Lett.,* **35,** L05307, doi:10.1029/2008GL033197.

Takeuchi, N., 2012. Detection of ridge-like structures in the Pacific Large Low-Shear-Velocity Province, *Earth planet. Sci. Lett.,* **319–320,** 55–64.

Tan, E., Leng, W., Zhong, S. & Gurnis, M., 2011. On the location of plumes and lateral movement of thermochemical structures with high bulk modulus in the 3-D compressible mantle, *Geochem. Geophys. Geosyst.,* **12,** Q07005, doi:10.1029/2011GC003665.

Tanaka, S., 2002. Very low shear wave velocity at the base of the mantle under the South Pacific Superswell, *Earth planet. Sci. Lett.,* **203,** 879–893.

Thorne, M.S., Garnero, E.J. & Grand, S.P., 2004. Geographic correlation between hot spots and deep mantle lateral shear-wave velocity gradients, *Phys. Earth planet. Inter.,* **146,** 47–63.

To, A., Romanowicz, B., Capdeville, Y. & Takeuchi, N., 2005. 3D effects of sharp boundaries at the borders of the African and Pacific Superplumes: observation and modeling, *Earth planet. Sci. Lett.,* **233,** 137–153.

Torsvik, T.H., Smethurst, M.A., Burke, K. & Steinberger, B., 2006. Large igneous provinces generated from the margins of the large low-velocity provinces in the deep mantle, *Geophys. J. Int.,* **167,** 1447–1460.

Wentzcovitch, R.M., Tsuchiya, T. & Tsuchiya, J., 2006. $MgSiO_3$ postperovskite at D″ conditions, *Proc. Nat. Acad. Sci. U. S. A.,* **103,** 543–546.

Wessel, P. & Smith, H.F.S., 1995. New version of the Generic Mapping Tools released, *EOS, Trans. Am. geophys. Un.,* **76,** 329.

## SUPPORTING INFORMATION

Additional Supporting Information may be found in the online version of this article:

**Figure S1.** Examples of accepted and rejected waveforms by applying the reading error estimation used in this study. A solid line in each panel represents the ScS waveform, which is overlaid by the S waveform (a waveform in red) at the time showing the maximum correlation coefficient. The reading errors of S and ScS phase are denoted with a red and blue straight lines at the peak amplitude of S and ScS, respectively, and the reading error of ScS–S is denoted at the left bottom of each panel. The event date, station name and the epicentral distance are displayed on the left top of each panel.

**Figure S2.** Example recording sections along longitude direction. The map on the left-hand side shows the ScS–S residuals (without correcting for mantle heterogeneity) for the example waveforms. Positive and negative residuals are plotted in the same manner as in Fig. 2a. Lines in colour show the ray paths where the ScS propagated through the lowermost 250 km of the mantle, with colours denoting the corresponding recording sections displayed on the right-hand panels. The right-hand panels show the recording sections of ScS. Each waveform is aligned by the expected arrival time of ScS calculated by PREM after being corrected for the observed S residual. Straight lines in red denote the observed arrival times of ScS measured by the cross-correlation.

**Figure S3.** Distribution of the synthetic and observed residuals for the tomography models (SMEAN, S362D1, SH18CEX and TXBW) and their best-scaled models. The maps are shown in the same manner as in Fig. 3a. The scaling factor for the best-scaled model is denoted in each model.

**Figure S4.** Average variances for the tomography models and their best-scaled models presented in Fig. S3. Symbols filled in colour denote the corresponding tomography models used for the modelling. A dotted red line shows the average variance for our preferred model (http://gji.oxfordjournals.org/lookup/suppl/doi:10.1093/gji/ggs002/-/DC1).

Please note: Oxford University Press are not responsible for the content or functionality of any supporting materials supplied by the authors. Any queries (other than missing material) should be directed to the corresponding author for the article.